INTERNATIONAL JOURNAL FOR NUMERICAL METHODS IN BIOMEDICAL ENGINEERING
Int. J. Numer. Meth. Biomed. Engng. 2012; **28**:697–713
Published online 28 March 2012 in Wiley Online Library (wileyonlinelibrary.com). DOI: 10.1002/cnm.2461

Sensitivity to outflow boundary conditions and level of geometry description for a cerebral aneurysm

S. Ramalho, A. Moura*,†, A.M. Gambaruto and A. Sequeira

Dept. of Mathematics and CEMAT/IST, Instituto Superior Técnico, Technical University of Lisbon, Av. Rovisco Pais 1, 1049-001 Lisboa, Portugal

SUMMARY

Mathematical models, namely the flow boundary conditions, as well as the detail of the bounding geometry, can highly influence the computed flow field. In this work, an anatomically realistic portion of cerebral vasculature with a saccular aneurysm, and its geometric idealisation, are considered. The importance of the geometric description, namely including the side branches or modelling them as holes in the main vessel, is studied. Several approaches to prescribe the outflow boundary conditions at the side branches are analysed, including the traction-free condition, zero velocity (hence neglecting the side-branch), and the coupling with simple zero-dimensional and one-dimensional models. Results of the effects of outflow boundary modelling choice on computed haemodynamic parameters are used to identify appropriateness of the models based on the physical interpretation. Estimated range of error-bars associated to outflow boundary model choice and the level of geometric details are presented for patient-specific computational haemodynamics, and can serve as invitation for future studies. The zero-dimensional and one-dimensional models are shown to provide good representations of the side branches in the case of the clipped geometry. Copyright © 2012 John Wiley & Sons, Ltd.

Received 29 June 2011; Revised 14 October 2011; Accepted 6 December 2011

KEY WORDS: cerebral aneurysm; computational fluid dynamics; outflow boundary conditions; geometrical multiscale modelling

1. INTRODUCTION

Intracranial aneurysms still represent a frightening and devastating silent threat, not only because they often remain asymptomatic until the time of rupture but also because of their association with high prevalence and mortality rates [1, 2]. The natural history of this pathology is far from fully understood, and its intricacies are reflected in the intensive multi-faceted and multi-disciplinary effort to understand the mechanisms involved in the developmental stages. Inherited and acquired factors may play a role in the aneurysm formation and rupture [3, 4], but specific haemodynamic characteristics, such as wall and oscillatory shear stress, elevated pressure, or flow impingement, are believed to be closely related with the aneurysm initiation and progression [5–8]. The importance of a detailed comprehension of the local blood flow conditions is clear, which can be useful for both diagnostic and treatment purposes. However, the current understanding of the factors and mechanisms linked to aneurysm formation and growth are limited, and at times, the conclusions are too restrictive and preclude direct use of numerical simulations in a clinical setting. Aneurysm studies are currently based on a variety of methodologies, including *in vitro* [9] and *in vivo* [10] models, and a great percentage relies on mathematical modelling and numerical simulations of blood flow in the aneurysm region, using both idealised and patient-specific geometries [8, 11–15].

*Correspondence to: A. Moura, Department of Mathematics , Instituto Superior Técnico, Technical University of Lisbon, Av. Rovisco Pais 1, 1049-001 Lisboa, Portugal.

†E-mail: almoura@math.ist.utl.pt

Patient-specific geometries can be highly irregular, with sharp curves, non-planarity and a large number of side branches, that lead to a complex flow field. The surrounding tissues such as the bone also play an important role in the shape and risk of rupture of aneurysms [16]. The strong dependence of the haemodynamics on the geometry makes it important to perform patient specific studies. However, the effect of the choice of mathematical models and parameters on the numerical solution is difficult to predict and usually requires a sensitivity analysis to estimate appropriate error bounds. This can be expensive, and idealised geometries are often used to test the impact of the modelling choice and the variation of some parameters at a lower computational cost, while giving a generalisation of the haemodynamics in anatomically realistic models. Prior to performing the simulations on realistic geometries, simplified symmetric geometries are appealing as an easier approach to conduct series of validation and optimisation tests, such as to assess the impact of the vessel curvature [15], presence of a side branch near the aneurysm [14], incrementation of the angle between parent vessel and aneurysm [13], or even to evaluate the performance of new image reconstruction methods [12]. On the other hand, patient-specific image-based CFD models benefit from being able to realistically reproduce the main haemodynamic features displayed in the aneurysm environment [6, 8]. Use of patient specific data obtained *in vivo* by means of non-invasive neuroimaging techniques has become routine and has allowed for the acquisition and processing of more accurate and detailed medical images. This is complemented by advances in high performance computers and efficient numerical algorithms that have led to more precise multi-physics results, able to efficiently simulate complex phenomena at high temporal and spatial resolutions. Despite the authenticity of the results, few studies have shown the association of modelling uncertainties with respect to the clinical data, concerning not only variations in the mathematical model but also in the computational model reconstruction [17–19].

The boundary condition choice may also introduce errors in the solution. It was reported in [20] that the shear stress distribution is sensitive to changes in the inflow parameters, and simplifications of the inflow conditions that may often be necessary owing to unavailable data, may lead to significant discrepancies between the haemodynamics *in vivo* and the computed flow field. Realistic inflow conditions, derived from phase-contrast MR imaging measurements in volunteers [8, 12, 21] can be a first approximation, however acquisition errors and artefacts are present. Owing to the scarcity of patient-specific flow conditions, many studies make further assumptions using mean flow conditions or typical velocity profiles [17, 22]. In [23], a relationship between flow rates and vessel areas in cerebral arteries was derived to allow for the comparison of haemodynamic variables between different cases. Similarly, the acquisition of flow rate measurements for the outflow sections also poses considerable difficulty, especially in the case of a ramified vessel. Many studies impose the dependence of the flow division among the downstream sections on the geometry, or prescribe traction free conditions [6, 20, 22]. However, a zero normal stress at all the outflow regions is far from reproducing a physiological situation. For instance, using compliant models with traction-free conditions at outflow causes the appearance of spurious and non-physiological reflections [24].

To properly account for the effects of the peripheral circulation and maintain a reasonable computational cost, reduced models such as one-dimensional (1D) and zero-dimensional (0D) models can be coupled to the three-dimensional (3D) domain in the truncated regions [24–28]. It is worth mentioning that the 1D models can act as absorbing boundary conditions, providing the appropriate pressure value at outflow, so that no spurious reflections appear [24]. Although the 0D models were difficult to set up owing to the choice of a large number of coefficients, they have been used to account for the whole circulatory system, predicting non intuitive accommodations of the human circulation in pathological cases [28], which otherwise could not be accounted for in numerical simulations.

When using patient-specific image-based CFD models, questions such as where to truncate the physical domain or which branches to include may be raised. The inclusion of insufficient neighbouring side branches may affect the CFD result [10], but the role of small vessels is often neglected [5, 6].

In the present work, a sensitivity analysis of the computed haemodynamics is performed for a set of outflow boundary conditions. The geometries considered are a patient-specific portion of the cerebral vasculature that contains a saccular aneurysm and its idealisation. The outflow sections

DOI: 10.1002/cnm

are ramifying side-branches from the main artery and are considered in two levels of detail: as 3D branches, or clipping these to leave holes in the main artery. The artery is assumed to be rigid and a steady flow regime is considered. A generalised Newtonian fluid model is used to account for the shear-thinning behaviour of blood [17, 24, 27].

Although a single data set is studied, comparison with the idealised geometry and generalisation of the findings to a larger data set assumes that the selection of suitable outflow conditions can be performed irrespective of other modelling conditions such as the inflow condition or rheological model of blood. This is a good hypothesis in the case of rigid walls; however, for unsteady simulations and compliant walls, this is not the case as reflecting waves will be generated at the outflow if care is not taken. The emphasis of this work is both to illustrate clearly different modelling choices for the outflow boundary conditions, and to compare the corresponding effects to identify their appropriateness, as well as to present the relative influence of each type of boundary condition on haemodynamic parameters. This sensitivity analysis estimates the respective error-bars associated to numerical simulations of haemodynamics with respect to a set of outflow boundary conditions.

The paper is structured as follows. Section 2 describes the medical image acquisition and the geometry reconstruction, as well as the definition of the idealised geometries. In Section 3, the 3D mathematical fluid model is presented, as well as several strategies for the outflow boundary conditions. The numerical simulations setup is introduced in Section 4, and in Section 5, the numerical results are illustrated and discussed. Conclusions are drawn in Section 6.

2. GEOMETRY RECONSTRUCTION

In this work, a CFD analysis is carried out to study the haemodynamics in cerebral aneurysms in a patient-specific geometry and its idealisation. The patient-specific geometry is reconstructed from medical images obtained *in vivo* from rotational computed tomography angiography, with resulting voxel resolution of 0.8 mm on a 256^3 grid. The reconstruction procedure of the 3D geometry surface for numerical simulations consists in image segmentation, surface extraction, and finally surface smoothing and meshing. A constant threshold value for segmenting the image data is used, and a marching tetrahedra algorithm is employed to extract the 3D surface that yields the initial triangulation. This approach is fast, but assumes that the image intensity of the desired object is sufficiently different from the background to permit a constant threshold choice. It also implies that the medical image resolution is fine enough to perform marching tetrahedra directly, instead of performing an interpolation [18, 29]. Several other segmentation methods exist for image data of cerebral aneurysms, and deformable models are commonly used [6, 30]. However, each method yields a different geometry definition that depends on user-defined coefficients and is ultimately limited by the acquisition modality, resolution, contrast and noise.

The resulting virtual model of the vasculature is then prepared for the numerical simulations by identifying the regions of interest and removing secondary branches. Surface smoothing is required owing to medical imaging noise and limited resolution that yields an initial surface definition, which is not anatomically representative. Smoothing is performed using the bi-Laplacian method, with a final inflation along the local normal by a constant distance to minimise the volume alteration and surface distortion [31]. The intensity of the smoothing is chosen to reduce the surface curvature variation with the constraint that alterations are under the voxel size, which is the basic unit size of uncertainty in interpreting the medical images.

Figure 1 shows the initial cerebral arterial geometry, with several secondary branches and a saccular aneurysm, as well as the region of interest that includes the aneurysm and the main side branches, and is used in the numerical simulations. For this patient specific data set, only side branches downstream of the aneurysm were identified from the medical images. Of these, three are located in the region of interest considered for the numerical simulations.

The idealisation of the patient-specific geometry of Figure 1 is performed using a relevant portion of the main vessel, including the aneurysm, and the thin side branch close to the aneurysm. Thus, the idealisation consists of a tube with constant circular cross-section that is either straight or has

DOI: 10.1002/cnm

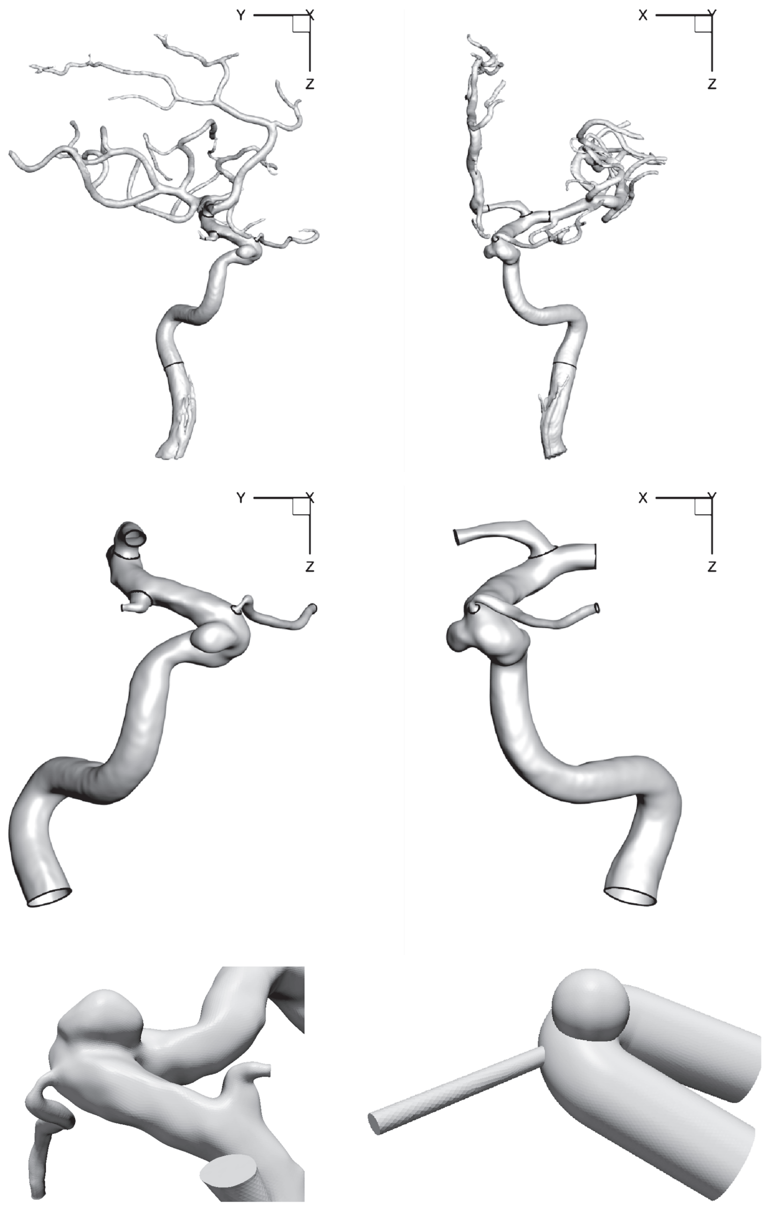

Figure 1. Reconstructed geometry (top row) and detailed view of region of interest (middle row), showing the different locations where the vessels are clipped. Left column is in the sagittal plane whereas the right column is in the coronal plane. Three side branches are present in the region of interest and located downstream of the aneurysm. Detail of the anatomically realistic geometry including the aneurysm (bottom left), and corresponding idealised geometry (bottom right).

a constant radius of curvature. The side branch is represented by a straight tube of constant cross-section, and the saccular aneurysm by a constant radius sphere (see Figure 1). Both the main vessel and the side branch are planar.

These idealisations appear to simplify the anatomically realistic geometry noticeably, maintaining only primitive information. The importance of considering idealised geometries relies in the fact that they provide a clearer understanding of the sensitivity of modelling choice (boundary conditions and level of geometry detail) to the computed flow field. In this work, the modelling choice is described by different outflow boundary conditions and by the level of geometry detail that should be included in the region of interest, particularly the inclusion or omission of portions of the side branches.

In this manner, a set of geometry definitions are setup that can be easily summarised as *realistic* or *idealised* geometries, each with *side branches* or *holes* for the outflow sections.

3. FLUID MODEL AND OUTFLOW BOUNDARY CONDITIONS

Blood is often considered a Newtonian fluid in large to medium vessels (for instance [12,23,28,31]); nonetheless, it exhibits non-Newtonian properties, mainly caused by the presence and rheological behaviour of red blood cells. In this work, the shear-thinning behaviour of blood will be considered, which is one of its main non-Newtonian properties, characterised by the decrease of the apparent viscosity with increasing shear rate. Given $\Omega \subset \mathbb{R}^3$ the open and bounded domain of interest, and $I = [0, T]$ the time interval, the momentum and continuity equations for incompressible and isothermal fluids are as follows:

$$\begin{cases} \rho\left(\dfrac{\partial \mathbf{u}}{\partial t} + \mathbf{u}\cdot\nabla\mathbf{u}\right) - \operatorname{div}\boldsymbol{\sigma}(\mathbf{u}, P) = \mathbf{0}, & \text{in } \Omega, \forall t \in I, \\ \operatorname{div}\mathbf{u} = 0, & \text{in } \Omega, \forall t \in I, \end{cases} \tag{1}$$

where ρ is the density of the fluid, and $\mathbf{u}$ and P are the unknown velocity and pressure, respectively. The Cauchy stress tensor $\boldsymbol{\sigma}(\mathbf{u}, P)$ is defined through a constitutive law, characterising the rheology of the fluid. A generalised Newtonian fluid will be considered, such that

$$\sigma(\mathbf{u}, P) = -P\mathbf{I} + 2\mu(\dot{\gamma})\mathbf{D}(\mathbf{u}), \tag{2}$$

where $\mathbf{D}$ is the strain rate tensor, given by $\mathbf{D}(\mathbf{u}) = \frac{1}{2}\left(\nabla\mathbf{u} + \nabla\mathbf{u}^T\right)$, and μ is the dynamic viscosity, which is assumed to depend monotonically on the shear rate $\dot{\gamma}$:

$$\dot{\gamma} = \sqrt{\frac{1}{2}\mathbf{D}(\mathbf{u}) : \mathbf{D}(\mathbf{u})}.$$

Different viscosity functions $\mu(\dot{\gamma})$ define different generalised Newtonian models, that can be of shear-thinning, shear-thickening, or yield stress type. Here, we consider the Carreau model, for which the viscosity function is given by

$$\mu(\dot{\gamma}) = \mu_\infty + (\mu_0 - \mu_\infty)\left(1 + (\lambda\dot{\gamma})^2\right)^{\frac{n-1}{2}}, \tag{3}$$

where $\lambda > 0$, and $n, \in \mathbb{R}$ are constants, and the coefficients μ_0 and μ_∞ are the asymptotic viscosity values at lower and higher shear rates, respectively. In this case, because the model is shear-thinning, $\mu_0 > \mu_\infty > 0$. All these parameters are obtained from curve fitting to experimental data. In particular, in this work, the parameter values of the viscosity function were estimated from experimental viscosity data obtained by Prof. M.V. Kameneva (Univ. Pittsburgh) for normal human blood (see [17,24] for details), and are given by $\mu_0 = 0.456$ P, $\mu_\infty = 0.032$ P, $\lambda = 10.03$ s and $n = 0.344$.

Equations (1) and (2) are endowed with the initial condition $\mathbf{u} = \mathbf{u}_0$, for $t = 0$, in Ω. The compliance of the artery wall is not accounted for, so that the domain is considered to be rigid and the no-slip condition $\mathbf{u} = \mathbf{0}$ is imposed on the physical wall boundary. At the inflow section, the flow rate, defined according to the cross-section area [23], is prescribed through a parabolic profile. At the artificial outflow sections, four different approaches are studied: traction free (zero normal stress), zero velocity (neglecting the side branch) and coupling with 1D and 0D reduced geometric multiscale models, that will now be discussed.

Firstly, the standard traction free or homogeneous Neumann boundary condition is considered in all outflow sections:

$$\sigma(\mathbf{u}, P)\cdot\mathbf{n} = \mathbf{0}, \tag{4}$$

where $\mathbf{n}$ is the outward unit normal to the section. This boundary condition will be always considered at the outflow section of the main vessel, also when other outflow conditions are taken for the

DOI: 10.1002/cnm

side branches. Secondly, the side branches will be neglected by imposing a zero velocity, $\mathbf{u} = \mathbf{0}$, on the side branches outflow boundaries.

Finally, the presence of the side branches is described by means of reduced 1D or 0D models, by making use of the so-called geometrical multiscale approach [26]. It consists of an hierarchical description, where the different parts of the circulatory system are modelled by different dimensional scales coupled together, corresponding to different levels of desired accuracy. Where high levels of detail are necessary, 3D models are used, whereas to account for the global circulation, reduced 1D or 0D models are coupled to the artificial boundary sections created from the truncation of the 3D domain (see Figure 2).

3.1. The 3D–1D coupling

The 1D model is obtained from the 3D fluid Equation (1), by assuming that the artery is a cylindrical compliant tube, with axial symmetry and fixed cylinder axis. The axial velocity is considered to be dominant, pressure is taken constant in each cross-section, and the wall displacements are only accounted for on the radial direction. The 1D model is then deduced by integrating in each cross section, assuming a uniform axial velocity profile although others can be used [26]. The result is a hyperbolic system of two equations, corresponding to the reduced form of the continuity and momentum equations:

$$\begin{cases} \dfrac{\partial A}{\partial t} + \dfrac{\partial Q}{\partial z} = 0, \\ \dfrac{\partial Q}{\partial t} + \dfrac{\partial}{\partial z}\left(\dfrac{\alpha Q^2}{A}\right) + \dfrac{A}{\rho}\dfrac{\partial \overline{p}}{\partial z} = -K_r \dfrac{Q}{A}, \end{cases} \quad ,z \in (a,b), t \in I, \tag{5}$$

where z is the axial coordinate, $L = b - a$ is the vessel length, and ρ is the constant fluid density. The momentum flux correction coefficient α (see [26] for its definition) is assumed to be constant $\alpha = 1$. Because in this work, a steady flow regime is considered, a parabolic velocity profile is assumed for the 1D model, corresponding to a parameter K_r defined by $K_r = 8\pi\mu$, where μ is the constant blood dynamic viscosity. Indeed, the 1D model (5) does not account for the shear-thinning behaviour of blood because it has been derived from the 3D fluid Newtonian model with a constant viscosity μ. Here, the 1D constant viscosity is considered to be $\mu = 0.04$ P, corresponding to the average experimental viscosity in the range of high shear rates $\dot{\gamma} \in [2, 1000]$ s^{-1} (see for instance [17, 24]). By changing the friction parameter K_r, other velocity profiles may be considered [32].

System (5) contains three unknowns, the cross-section area $A(t,z)$, the flow rate $Q(t,z)$, and the mean pressure $\bar{p}(t,z)$, and only two equations. To close the system we assume that the external pressure is zero and consider a simple algebraic expression relating the blood mean pressure and the area [26, 33], accounting for radial displacements only and neglecting inertial terms:

$$\overline{p} = \beta \frac{\sqrt{A} - \sqrt{A_0}}{A_0}, \quad \text{where} \quad \beta = \frac{\sqrt{\pi} h_0 E}{1 - \xi^2}, \tag{6}$$

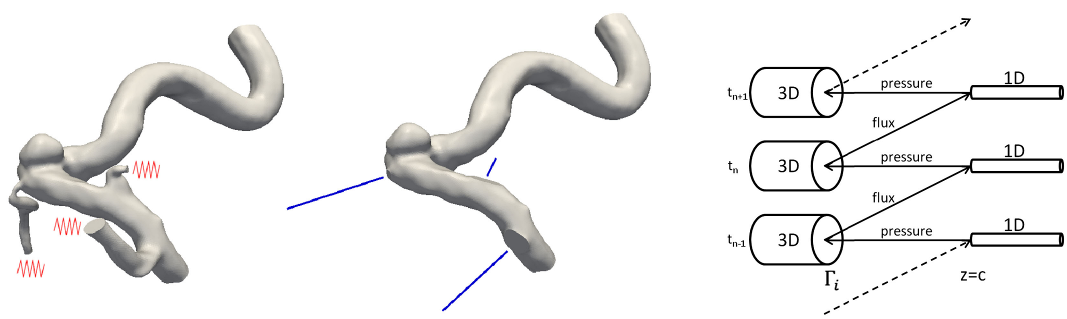

Figure 2. Schematic of the coupling with the zero-dimensional model (left) and the one-dimensional model (centre). Scheme of the explicit coupling between the three-dimensional and one-dimensional models (right).

where A_0 and h_0 are the cross-section area and wall thickness at rest, respectively, E is the Young modulus, and ξ the Poisson ration. Thus, the coefficient β concentrates the mechanical properties of the vessel wall. Both A_0 and β may vary along the vessel length z; however, here, we consider them to be constant. Systems (5) and (6) are provided with proper initial and boundary conditions.

The 1D model is then composed of Equations (5) and (6). It captures very well the pulse propagation nature of blood flow in arteries [34, 35], and it has been validated against *in vitro* experimental data [32]. The 1D models are well adapted to study the arterial wave propagation in large arterial networks, owing to their low computational cost, enabling a better understanding of the function of the cardiovascular system both in healthy and pathological cases (see [34] for a recent review on 1D pulse wave propagation models of the arterial system). In this work, the 1D model is coupled to the 3D problem, where the region of interest includes the aneurysm, and it acts as auxiliary by providing proper outflow conditions to the 3D model. The 1D model will be coupled to the 3D rigid model only on the clipped geometries, on the cross sections generated by the crop of the side branches, as illustrated in Figure 2 (middle). Hence, the side branches will be considered as 1D models, and as discussed in the results, some physical properties such as pressure drops across the branches are well approximated by the 1D models. Although the 1D system (5) is a compliant model for blood flow in arteries, and the 3D model is rigid, there is no problem regarding pressure waves reflections because the 1D model outflow sections are set to be absorbing.

The 3D–1D coupling is performed by imposing, at the coupling section interface, the continuity of the flow rate and of the mean pressure [33], noticing that the diffusion term on the 1D momentum equation is a simple friction parameter:

$$-\boldsymbol{\sigma}\cdot\mathbf{n} = P\mathbf{n} - 2\nu\mathbf{D}(\mathbf{u})\cdot\mathbf{n} = \overline{p}_{1\mathrm{D}}\mathbf{n}, \tag{7}$$

$$Q_{3\mathrm{D}} = \int_{\Gamma_a^t} \mathbf{u}\cdot\mathbf{n}\,\mathrm{d}\gamma = Q_{1\mathrm{D}}. \tag{8}$$

Precisely, the 3D–1D coupling is carried out in an explicit manner, prescribing (8) on the 1D model by computing the flow rate on the 3D outflow coupling section at the previous time, and imposing (7) on the 3D model as a Neumann boundary condition at the current time (see Figure 2 (right)).

3.2. *The 3D–0D coupling*

Lumped parameter models are derived from the 1D model by further averaging in space [26, 28], losing dependence of the spatial coordinate, and hence, are denoted as 0D models. They consist of a system of ordinary differential equations describing the variations in time of the mean pressure and flow rate in certain compartments of the cardiovascular system, such as the heart, the venous bed, or the pulmonary circulation. For that reason, coupling them with the 3D model allows to account for the global circulation. The 0D models are analogous to electrical networks, the flow rate being analogous to the current, the mean pressure to the voltage, the blood viscosity to the resistance, the blood inertia to the inductance, and the wall compliance to the capacitance.

In this study, a very simple lumped parameter model of a simple resistance will be used, consisting of an algebraic relation between the flux and the mean pressure through the resistance parameter: $P = RQ$. The resistance parameter R is chosen following [24], and will now be briefly described.

The 1D system of Equation (5) is hyperbolic and possesses two distinct eigenvalues $\lambda_{1,2} = \overline{u} \pm \sqrt{\frac{\beta}{2\rho A_0}}A^{\frac{1}{4}}$, where $\overline{u} = \frac{Q}{A}$ is the mean velocity. The associated eigenfunctions or characteristic variables are given by

$$W_{1,2}(Q, A) = \overline{u} \pm 4\sqrt{\frac{\beta}{2\rho A_0}}\left(A^{\frac{1}{4}} - A_0^{\frac{1}{4}}\right). \tag{9}$$

Under physiological conditions in haemodynamics, the eigenvalues $\lambda_{1,2}$ have opposite signs, and W_1 and W_2 correspond to the incoming characteristics at the left (inflow) and right (outflow) extremities of the 1D tube, respectively [26]. Notice that $W_{1,2} = 0$ for $A = A_0$ and $Q = 0$, that is, at rest.

DOI: 10.1002/cnm

Imposing the incoming characteristic on the outflow point W_2 to be zero, corresponds to an absorbing boundary condition because it means there are no waves incoming the domain [24, 33]. From expression (9), imposing $W_2(\bar{p}, Q) = 0$ is equivalent to imposing [24]:

$$\sqrt{\frac{8\beta}{\rho A_0}}\left(\bar{p}\frac{A_0}{\beta} + \sqrt{A_0}\right)^2 \left(\sqrt{\bar{p}\frac{A_0}{\beta} + \sqrt{A_0}} - A_0^{1/4}\right) = Q, \tag{10}$$

and performing a linearisation by considering the first-order term of a Taylor expansion around zero, the following expression relating the mean pressure and the flow rate is obtained [24]:

$$Q \approx \frac{\sqrt{2}A_0^{5/4}}{\sqrt{\rho\beta}}\,\bar{p}. \tag{11}$$

This is a good approximation of (10) as long as the Young modulus is sufficiently high [24]. Namely, it is valid for physiological wall stiffness. The 0D resistance thus considered is given by $R = \frac{\sqrt{\rho\beta}}{\sqrt{2}A_0^{5/4}}$.

In a similar manner to the 3D–1D coupling, the 3D–0D coupling is performed explicitly, making use of the flow rate computed from the 3D at the previous time step to compute the mean pressure at the current time step through (11), and prescribe it as a constant Neumann boundary condition on the 3D coupling interface section:

$$\bar{p}^{(n+1)} \approx \frac{\sqrt{\rho\beta}}{\sqrt{2}A_0^{5/4}}\,Q^{(n)}.$$

Notice that the resistance parameter thus considered captures the absorption properties of the 1D model, but does not correspond to the equivalent resistance of the 1D tube because the length is not accounted for. To account for the resistance of the 1D tube, the equivalent lumped parameter model should include inductance and compliance as well as resistance. This could be easily carried out (following for instance [27]), but there would not be expected differences between the 3D–1D and the 3D–0D coupling approaches. There are other, more sophisticated 0D models that might be used such as the ones presented in [25, 28] that realistically account for flux and mean pressure variations in specific compartments of the cardiovascular system. These are more accurate but also more complex, and require setting proper lumped parameters that are difficult to obtain for patient specific studies, and will not be addressed here. In [35], the coupling of different 0D models into the 1D problem has been carried out, and their influence into the 1D pulse wave form analysed. In this work, the coupling of 0D models to the 1D problem is not addressed, and the simple absorbing outflow boundary condition $W_2(Q, A) = 0$ is prescribed at the 1D outflow.

4. NUMERICAL SIMULATIONS SETUP

The simulations were carried out using a patient-specific geometry and an idealisation of a portion including the aneurysm and the closest side branch, as depicted in Figure 3. Geometrical variations entail including or omitting reconstructed portions of the side branches, for both the patient-specific and idealised geometries. This resulted in a total of four different geometries. The four different types of outflow boundary conditions described in Section 3 were considered on the side branches: zero velocity (meaning the side branch is neglected); zero normal stress; coupling with the 0D model; and finally the coupling with a 1D model of the same length of the side branch (hence, only applied in the clipped geometries). As mentioned, in order to make comparisons between each computed solution at the outflow of the main vessel, a zero stress condition (4) was consistently applied.

The numerical solution of the 3D fluid Equations (1) and (2) was obtained using the LifeV finite element library (`lifev.org`, see for instance [33, 36]), with in-house extensions. The discretisation in time was performed by means of a backward Euler scheme. The space discretisation was carried out resorting to $P1 - P1$ elements, using streamline diffusion stabilisation [37]. Regarding

DOI: 10.1002/cnm

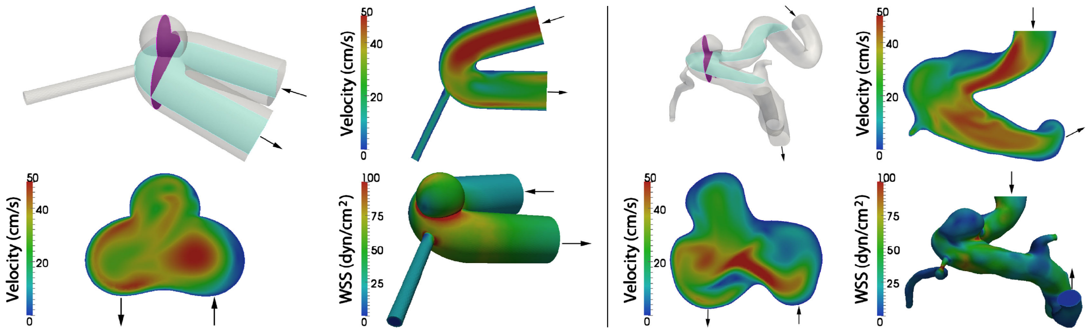

Figure 3. Geometries including the side branches coupled with a zero-dimensional model ($_{br}$0D) with arrows to indicate flow direction. Illustration of the chosen cross sections (top-left), velocity magnitude (cm/s) in both cross section (top-right and bottom-left), and wall shear stress magnitude (dyn/cm^2) (bottom-right). Note that for the velocity cross section that includes the aneurysm, the upstream flow is on the right and the downstream flow on the left.

the 1D model, the Lax–Wendroff scheme was applied for the time discretisation and P1 finite elements were considered for the space approximation [26]. The Lax–Wendroff scheme is explicit, so a CFL condition must be verified for the 1D model. This results in a smaller time step for the 1D model than for the 3D domain, such that two different time steps are used. The 1D model advances in time with a smaller time step and the same boundary conditions until it reaches synchronisation with the time interval used to resolve the 3D domain.

At each time step, a steady state inflow regime is imposed at the inflow section as a parabolic profile. The reference value for the inflow condition was obtained through the relationship between flow rate and vessel area, derived from measurements in internal carotid and vertebral arteries [23]. The area of the inflow section of the idealised configuration is naturally smaller than the inflow section of the patient-specific geometry, because it lies downstream. However, for comparison purposes, and because in this work, no side branches are present upstream of the aneurysm, the same flow rate is prescribed in both geometries. Given the relation $Q = k \cdot A^n$ with the constants $k = 48.21$, and $n = 1.84$ (see [23]), and the area of the inflow section of the anatomically realistic geometry, $A = 0.208$ cm^2, the prescribed inflow steady flux is $Q = 2.67$ cm^{3}s^{-1}. A ramp on the inflow flux is used, starting from the initial rest state $Q = 0$ cm^{3}s^{-1} and using $Q_{\text{in}}^{\text{ramp}}(t) = \frac{t\,Q}{t_{\text{ramp}}}$, for $t < t_{\text{ramp}}$, with the time length of the ramp chosen to be $t_{\text{ramp}} = 0.01$ s. The computations were run until steady state was reached, identified by negligible differences O(10^{-10}), in the solution. In all cases, the simulations were carried out using a time step of 10^{-3} s on the 3D model, whereas a time step of 0.5×10^{-4} s was taken for the 1D model.

Steady state results, while a limitation and non-physiological, were used to identify with greater clarity effects of the outflow boundary conditions in a problem of reduced complexity. Moreover, rotational CT angiography scans give good contrast and resolution to identify the arteries in the region of interest; however, no flow velocity data is provided to be able to set the inflow boundary conditions appropriately. In this work, a suitable flow rate was imposed at inflow using the work of Cebral *et al*. [23]; however, other studies have shown the influence of varying the flow rate on the haemodynamics in the cerebral aneurysms [38]. This has been avoided here as there is an inherent modelling uncertainty in imposing time-varying inflow boundary conditions. Nevertheless it is of interest in future work to study the effects of the outflow boundary conditions on unsteady simulations.

Concerning the 1D hyperbolic model, an absorbing boundary condition $W_2 = 0$, was considered at the downstream section of the 1D domain. For both 1D and 0D models, the β parameters used were determined through Equation (6), where the thickness of the wall h_0 was set to be 10% of the vessel radius, the Young Modulus $E = 10^5$ dyn/cm^2, and the Poisson ratio is set to $\xi = 0.5$ (assuming that the artery wall is incompressible). It should be noted that the Young Modulus used here is an order of magnitude smaller than that reported in the literature [33, 35] because this was seen to

DOI: 10.1002/cnm

improve the stability of the simulations. Nevertheless, some numerical tests on the idealised geometry using a Young Modulus one order higher were carried out, and the solution was not affected because steady state solutions are sought in the current work, and hence, the reduced models act as rigid tubes with auto-regulated absorbing outflow resistances. As described in Section 3, the coupling of the 3D fluid model with the reduced 1D and 0D models is performed by means of an explicit algorithm, and the defective mean pressure data provided by the reduced model is imposed on the outflow section of the 3D model through a Neumann boundary condition (see [33] and references therein regarding defective boundary data).

The simulations considering the patient-specific geometry with the side branches were performed using a graded mesh with element size of 0.02 cm within the aneurysm, and maximum size of 0.05 cm, amounting to using around 1.9 M tetrahedral elements. Regarding the clipped patient-specific geometry, a finite element mesh of about 1.2 M tetrahedra was employed, corresponding to a maximum element size of 0.04 cm. Concerning the idealised configurations, both branched and clipped geometry meshes were composed of approximately 1.1 M tetrahedral elements, corresponding to a maximum size of 0.04 cm.

5. RESULTS AND DISCUSSION

The results are presented for the entire geometry unless explicitly stated, in which the flow within the aneurysm or a cross section is considered. The following abbreviations of the boundary conditions imposed are used: TF for traction free conditions, V0 for no-slip velocity, 0D for the 0D resistance model, 1D for the 1D model. Furthermore, the subscripts (cl) and (br) are used to indicate if the geometry is *clipped* or has *branches*, respectively. For example, ${}_{br}$0D indicates that the geometry includes side branches to which the 0D model is coupled, as illustrated in Figure 3. In this figure, the locations of the cross sections are identified.

In Figure 3, velocity cross sections and WSS distributions are shown for ${}_{br}$0D, whereas in Figure 4, the WSS distribution and velocity pathlines for ${}_{br}$TF and ${}_{cl}$TF are shown, for both the idealised and realistic geometries. Clear differences are visible, and importantly, within the aneurysm, the realistic geometry has lower WSS and velocity magnitude than its idealisation. Downstream of the aneurysm, the velocity magnitude decreases abruptly in the idealised geometry, contrary to the realistic one. The large differences seen are likely attributable to the reduced detail of the idealised geometry and the simplified inflow velocity profile imposed that varies significantly to that of the realistic geometry at the same section. The local changes in vessel surface for the realistic geometry allow for a more complex flow field, as shown by the velocity cross sections and pathlines, with a reduced presence of larger flow structures and a reduced WSS. Despite these differences, however, some features between the realistic geometry and its idealisation are comparable such as the flow split in the first side branch (detailed in Table I), which is 2% and 1% respectively for ${}_{br}$0D, and 3%

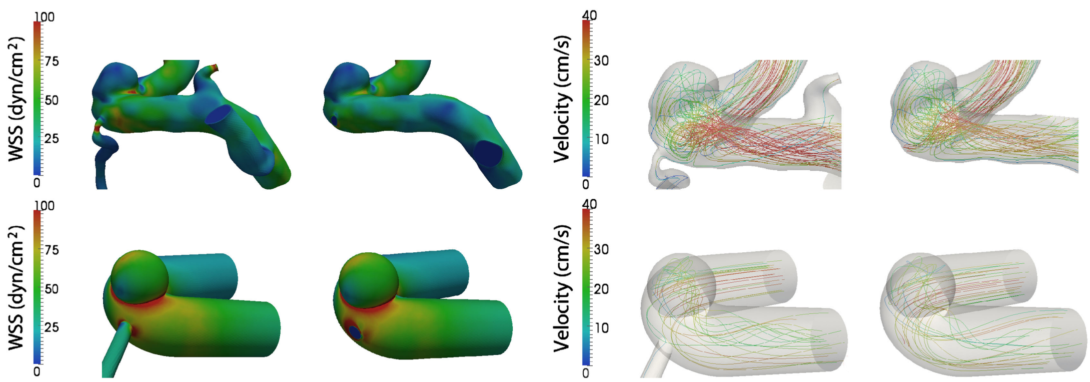

Figure 4. Distribution of wall shear stress magnitude (dyn/cm^2) and velocity pathlines (coloured by velocity magnitude) on the anatomically realistic (top row) and idealised (bottom row) geometries with and without side branches, using the traction-free boundary condition, hence ${}_{cl}$TF and ${}_{br}$TF.

DOI: 10.1002/cnm

Table I. Left: pressure drop (dyn/cm^2, where 10 dyn/cm^2 = 1 Pa), and right: flow rate division for the first side branch (percentage with respect to the inflow flux), for different geometries. For each case, the first row presents these results between the inflow section and the end of the first side branch, whereas the second row relates the inflow and outflow sections of the main vessel.

		TF (dyn/cm^2/%)	V0 (dyn/cm^2/%)	0D (dyn/cm^2/%)	1D (dyn/cm^2/%)
Idealised	Clipped	1054/8 1095/92	−263/0 1163/100	9/3 1134/97	−32/3 1136/97
	With branch	1129/2 1143/98	−390/0 1160/100	624/1 1149/99	
Real	Clipped	2612/16 2609/38	1581/0 4000/100	1846/8 3176/66	2193/12 3020/60
	With branch	3616/3*l* 3620/83	1573/0 4059/100	3411/2 3802/90	

and 2% for ${}_{br}$TF, whereas in the clipped case, greater differences are seen with 8% and 3% for ${}_{cl}$0D and 16% and 8% for ${}_{cl}$TF.

In Table I, the pressure drop values between the inflow and the first side branch are also presented, as well as between the inflow and the outflow of the main vessel. At first glance, it is apparent that the traction-free boundary condition is almost equivalent to imposing a pressure, giving approximately the same pressure drop between inflow and the side branch or main vessel outflows. The traction-free boundary condition hence assumes that the pressure at all outlets is approximately the same, if the flow is relatively developed. Physically, this is equivalent to assuming that the same level of the cardiovascular tree is reached at these outflow sections, which is not physiological. For the idealised geometry, the pressure drop between the inflow and the main vessel outflow remains relatively constant for different outflow boundary conditions, whereas that at the side branch changes significantly, resulting in a substantial flow split difference. For the anatomically realistic geometry, a greater difference is seen in pressure drops in general; however, the 0D and 1D models respond similarly. The no-slip condition causes a greater pressure drop to the main vessel outflow because of the increased flux in the main vessel. In the clipped case of the realistic geometry, the traction-free boundary condition causes a large flux to exit the side branch, whereas the 0D and 1D give a better representation. It is important to note that the no-slip boundary condition on the clipped realistic geometry yields a flow split closer to the realistic geometry with branches because of the high flow resistance of the first side branch owing to its tortuosity and presence of a stenosis.

The differences in the computed solutions preclude a direct quantitative analysis, so that the realistic and idealised geometries will be compared qualitatively. The idealisation serves as an approximate solution to the realistic case, with the advantage that the simplified form will emphasise the effects of varying the outflow boundary conditions. This is due to a representative flow field in the idealised geometry, with reduced presence of complex secondary flows.

The following results presented focus on the differences in the computed solutions and are based on the perspective of an end user who wishes to perform numerical simulations of haemodynamics in large arteries, with physiological relevance. Thus, the effects of different branch outflow boundary conditions are compared with the traction-free boundary condition, as this is the most commonly used in the literature.

Taking the geometries with clipped branches as reference, selected results are presented in Figures 5–7. The values of differences in velocity and WSS magnitude are presented in Table II. From the WSS map (Figure 5) and velocity cross sections (Figures 6 and 7), it is apparent that the ${}_{cl}$1D–${}_{cl}$0D comparison presents small differences in the flow field, as expected, whereas ${}_{cl}$TF–${}_{cl}$V0 presents the greatest difference both in the vessel and aneurysm. These results are common to both the realistic and idealised geometries; however, a noticeable difference appears in ${}_{cl}$1D–${}_{cl}$0D for the realistic geometry. To clarify this difference, one should recollect that the 0D model corresponds to

DOI: 10.1002/cnm

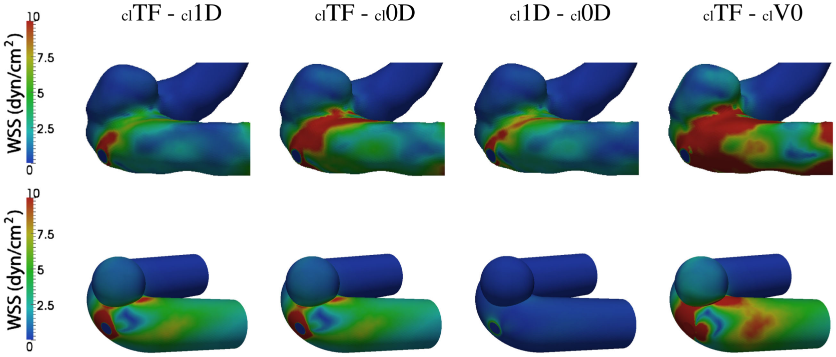

Figure 5. Differences of the wall shear stress magnitude (dyn/cm^2) between different boundary conditions using the anatomically realistic (top row) and idealised (bottom row) geometries without side branches.

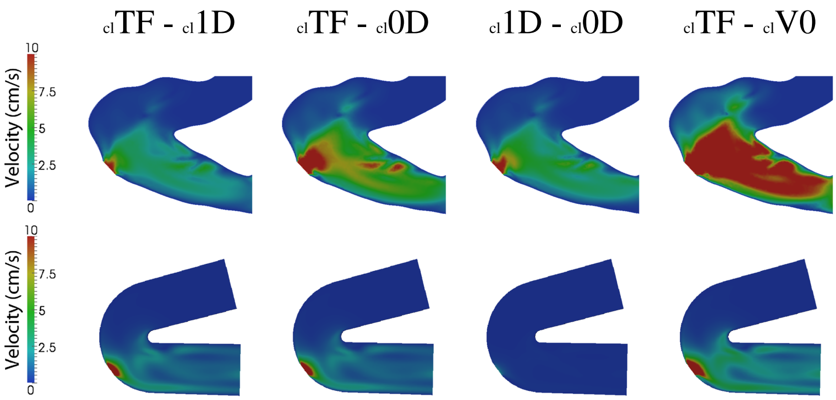

Figure 6. Cross section (planar) of differences of the velocity magnitude (cm/s) between different boundary conditions using the anatomically realistic (top row) and idealised (bottom row) geometries without side branches.

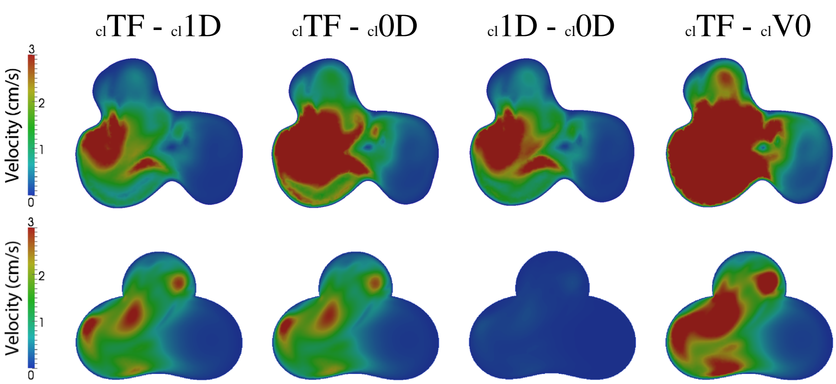

Figure 7. Cross section (transverse) of differences of the velocity magnitude (cm/s) between different boundary conditions using the anatomically realistic (top row) and idealised (bottom row) geometries without side branches.

imposing a zero incoming characteristic of the 1D model directly at the interface section, so that its resistance represents the absorption of the corresponding 1D wave. However, as already mentioned in Section 3.2, it does not coincide with the resistance of the 1D tube, nor take into account its length.

Considering as reference a geometry with side branches and traction-free boundary condition ($_{\text{br}}$TF), a comparison with clipped geometries and different outflow conditions is now undertaken.

DOI: 10.1002/cnm

Selected results are displayed in Figures 8–10, whereas the respective differences are presented in Table III. From the WSS map (Figure 8) and the velocity cross sections (Figures 9 and 10), the comparison of $_{br}$TF–$_{cl}$1D and $_{br}$TF–$_{cl}$0D result in the smallest differences of the flow field for the idealised configuration, whereas $_{br}$TF–$_{cl}$TF has the greatest differences in both geometries. This is also mirrored in the flow division as shown in Table I.

Table II. Comparison between different boundary conditions using a clipped geometry. The maximum difference for the velocity is calculated for the planar cross section, using the maximum inflow value for the percentage calculation. The maximum difference for the WSS is for the whole geometry.

	Test case	Velocity Max diff	Velocity Mean diff	WSS Max diff	WSS Mean diff
Idealised	$_{cl}$TF–$_{cl}$1D	35 (141%)	0.5440	146 (99%)	0.0050
	$_{cl}$TF–$_{cl}$0D	33 (133%)	0.5130	139 (95%)	0.0050
	$_{cl}$1D–$_{cl}$0D	2 (9%)	0.0300	7 (5%)	0.0003
	$_{cl}$TF–$_{cl}$V0	63 (251%)	0.8450	236 (161%)	0.0080
Realistic	$_{cl}$TF–$_{cl}$1D	12 (49%)	0.7910	29 (20%)	0.0120
	$_{cl}$TF–$_{cl}$0D	27 (107%)	1.1770	43 (29%)	0.0180
	$_{cl}$1D–$_{cl}$0D	15 (60%)	0.3860	23 (16%)	0.0050
	$_{cl}$TF–$_{cl}$V0	55 (221%)	2.5790	79 (54%)	0.0380

WSS, wall shear stress; TF, traction free.

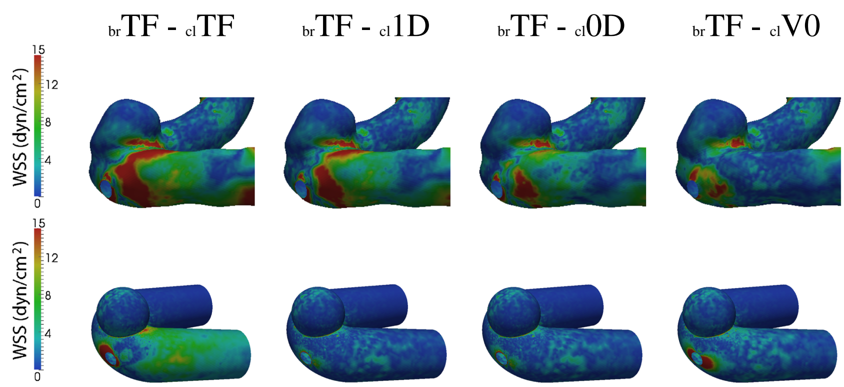

Figure 8. Differences of the wall shear stress magnitude (dyn/cm^2) between the anatomically realistic and idealised geometries with and without side branches.

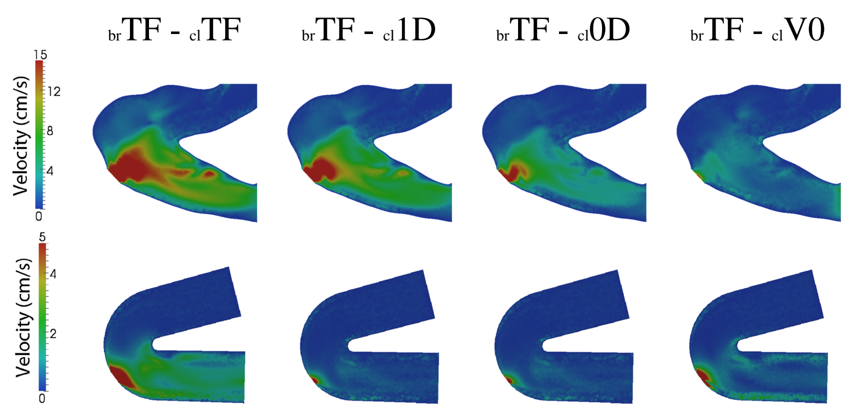

Figure 9. Cross section (planar) of differences of the velocity magnitude (cm/s) between the anatomically realistic and idealised geometries with and without side branches.

DOI: 10.1002/cnm

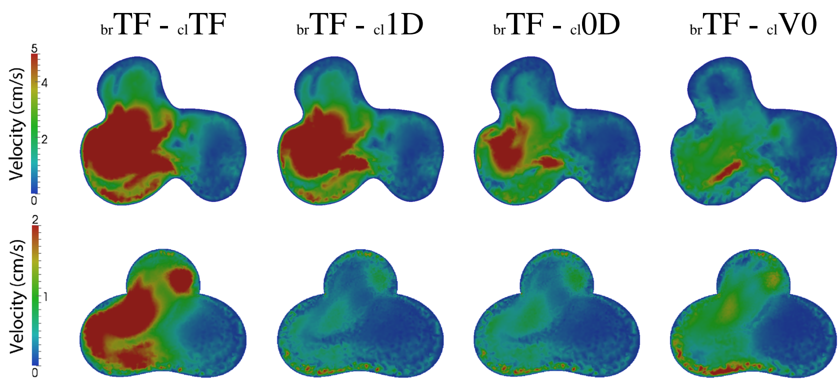

Figure 10. Cross section (transverse) of differences of the velocity magnitude (cm/s) between the anatomically realistic and idealised geometries with and without side branches.

Table III. Comparison between different boundary conditions using the geometries with and without side branches. The maximum difference for the velocity is calculated for the planar cross section, using the maximum inflow value for the percentage calculation. The maximum difference for the WSS is for the whole geometry.

	Test case	Velocity: Max diff	Velocity: Mean diff	WSS: Max diff	WSS: Mean diff
Idealised	$_{br}$TF–$_{cl}$TF	57 (229%)	0.528	206 (140%)	1.95
	$_{br}$TF–$_{cl}$1D	29 (115%)	0.016	61 (42%)	0.71
	$_{br}$TF–$_{cl}$0D	31 (123%)	0.014	68 (46%)	0.76
	$_{br}$TF–$_{cl}$V0	30 (121%)	0.320	78 (53%)	0.98
Realistic	$_{br}$TF–$_{cl}$TF	48 (191%)	1.904	61 (41%)	6.23
	$_{br}$TF–$_{cl}$1D	38 (151%)	1.113	51 (34%)	4.29
	$_{br}$TF–$_{cl}$0D	25 (99%)	0.727	46 (31%)	3.39
	$_{br}$TF–$_{cl}$V0	14 (57%)	0.675	44 (30%)	3.05

When considering the geometry with side branches, the influence of the different boundary conditions is not readily carried through from the realistic to idealised case, unlike when comparing the boundary conditions for the clipped geometry. The principal reason for this is the complex shape of the side branches and their tapering, not taken into account in the idealised geometry. This implies that, although the 1D reduced model parameters (straight tube of constant radius and length) correspond to the side branch of the idealised geometry, it is not the case for the realistic one. In the case of the 1D and 0D couplings, the boundary conditions applied to the clipped geometry depend locally on the area of the side branch at the point of departure from the main vessel, and do not take into account the drastic reduction of the side branches area downstream. Similarly, the shape of the side branches is not considered in the 1D and 0D models, namely curvature and non planarity. This results in large discrepancies when comparing $_{br}$TF with $_{cl}$1D and $_{cl}$0D. In the case of the $_{br}$TF–$_{cl}$V0 comparison, the differences are relatively small because of the stenosis in the first side branch that greatly reduces the flow in it. That is also seen by the flow division in the first side branch for the realistic geometry: 3% for $_{br}$TF, and 0%, 8% and 12% for $_{cl}$V0, $_{cl}$0D and $_{cl}$1D, respectively (see Table I). In this case, including the tapering of the vessel on the 1D problem, at the cost of increasing the 1D model complexity would lead to better results for the 1D coupling strategy.

It is therefore difficult to infer an appropriate boundary condition model for the outflow sections in the case of a clipped geometry where the downstream branch geometry is not known, as may occur if the branch is not reconstructed because of poor image contrast or resolution. It is also apparent that the traction-free boundary condition is not a good representation in the clipped geometry, and considering it is non-physiological in the branch geometry as it assumes approximately equal pressure, so it should be used with care. In general, the 0D and 1D models perform best, although still underlining uncertainty in modelling choice.

DOI: 10.1002/cnm

6. CONCLUSIONS

In this work, an anatomically realistic geometry of a cerebral aneurysm and its idealisation were considered to study the importance of outflow boundary conditions. This was performed at two levels. Firstly, considering the geometric detail of the side branches, using either the reconstructed surface or clipping these to leave only holes in the main vessel. Secondly, by considering a set of four different outflow boundary condition models: traction-free (TF), zero velocity (V0), coupling with a 0D resistance (0D), and coupling with a 1D model (1D) with the side branch length. The latter was enforced only on the geometry where the side branches were not included on the 3D model, substituting the side branch.

The idealised geometry was planar and had a constant cross-sectional area and radius of curvature of the bend. It was used to reduce the complexity of the flow field, and it provided a clearer understanding of the influence of the side branches as well as the different outflow boundary conditions applied. It was shown that the reduced models are promising in accounting for the side branches, providing a reasonable pressure drop at the branch outflow sections.

Concerning the anatomically realistic geometry, the results are comparable to its idealisation on the whole, with similar trends in the variability of the computed flow field regarding the changes in the outflow conditions. Nevertheless, a direct correspondence is difficult to establish because the flow field is locally different. The reported effects of the different outflow boundary conditions can be considered for other patient-specific cases; however, because the flow field will be different, the results presented here cannot be simply scaled and the effects may be more general. In this respect, a study with larger number of geometries is necessary.

In the case of the side branch on the 3D model with several boundary condition approaches, the TF and 0D models provide similar results. Comparing the results of the 3D side branch with those of the clipped geometry, the 0D and 1D models yield the closest solutions to the 3D branch. Nonetheless, these reduced models do not take into account the change in cross-sectional area nor the tortuous shape of the side branches. Namely, the anatomically realistic side branches for the case studied exhibit strong tapering and curvature, which highly influences the flow. To reflect these geometric characteristics, a more sophisticated 1D model can be derived; however, it will be necessary to reconstruct the side branches to do this, which may not always be possible or feasible. Correspondingly, this would also lead to a different resistance on the 0D model that is derived as the leading linear term in the series expansion.

As main conclusion, the 0D and 1D models seem to be the more appropriate outflow boundary conditions. This is true when the side branches are reconstructed and the models are used to substitute these, or if no downstream information is known. Clearly, the results in this work demonstrate that in both cases of realistic and idealised geometries, the prescription of outflow conditions is very important, highly influencing the haemodynamics inside the aneurysm, and they should be chosen with special caution. Future work should also include a time-varying inflow boundary condition to study the effect on a realistic flow waveform.

ACKNOWLEDGEMENT

We greatly acknowledge Prof. Jorge Campos and his team, from the Faculty of Medicine of the University of Lisbon, for providing us the *in vivo* rotational CTA scans of specific patients. This work has been partially funded by FCT (Fundação para a Ciência e Tecnologia, Portugal) through grants SFRH/BPD/34273/2006 and SFRH/BPD/44478/2008, and through the project UTAustin/CA/0047/2008.

REFERENCES

1. Krex D, Schackert HK, Schackert G. Genesis of cerebral aneurysms—an update. *Acta Neurochirurgica* 2001; **143**(5):429–49.
2. Rinkel GJE, Djibuti M, Algra A, Van Gijn J. Prevalence and risk of rupture of intracranial aneurysms: a systematic review. *Stroke* 1998; **29**(1):251–56.

DOI: 10.1002/cnm

3. Onda H, Kasuya H, Yoneyama T, Takakura K, Hori T, Takeda J, Nakajima T, Inoue I. Genomewide-linkage and haplotype-association studies map intracranial aneurysm to chromosome 7q11. *The American Journal of Human Genetics* 2001; **69**(4):804–19.
4. Pope FM, Narcisi P, Neil-Dwyer G, Nicholls AC, Bartlett J, Doshi B. Some patients with cerebral aneurysms are deficient in type III collagen. *The Lancet* 1981; **317**(8227):973–75.
5. Baek H, Jayaraman MV, Richardson PD, Karniadakis GE. Flow instability and wall shear stress variation in intracranial aneurysms. *Journal of The Royal Society Interface* 2010; **7**(47):967–88.
6. Cebral JR, Castro MA, Appanaboyina S, Putman CM, Millan D, Frangi AF. Efficient pipeline for image-based patient-specific analysis of cerebral aneurysm haemodynamics: technique and sensitivity. *IEEE Transactions on Medical Imaging* 2005; **24**(4):457–67.
7. Meng H, Wang Z, Hoi Y, Gao L, Metaxa E, Swartz DD, Kolega J. Complex haemodynamics at the apex of an arterial bifurcation induces vascular remodeling resembling cerebral aneurysm initiation. *Stroke* 2007; **38**(6):1924–31.
8. Steinman D, Milner J, Norley C, Lownie S, Holdsworth D. Image-based computational simulation of flow dynamics in a giant intracranial aneurysm. *American Journal of Neuroradiology* 2003; **24**:55966.
9. Imbesi SG, Kerber CW. Analysis of slipstream flow in a wide-necked basilar artery aneurysm: evaluation of potential treatment regimens. *American Journal of Neuroradiology* 2001; **22**(4):721–24.
10. Zeng Z, David FK, Durika M, Ding Y, Lewis DA, Kadirvel R, Robertson AM. Sensitivity of CFD based hemodynamic results in rabbit aneurysm models to idealizations in surrounding vasculature. *Journal of Biomechanical Engineering* 2010; **132**(9):091009.
11. Burleson AC, Strother CM, Turitto VT. Computer modeling of intracranial saccular and lateral aneurysms for the study of their haemodynamics. *Neurosurgery* 1995; **37**(4):77484.
12. Castro MA, Putman CM, Cebral JR. Patient-specific computational modeling of cerebral aneurysms with multiple avenues of flow from 3D rotational angiography images. *Acad Radiol* 2006; **13**:81121.
13. Ford MD, Lee SW, Lownie SP, Holdsworth DW, Steinman DA. On the effect of parent-aneurysm angle on flow patterns in basilar tip aneurysms: towards a surrogate geometric marker of intra-aneurismal haemodynamics. *Journal of Biomechanics* 2008; **41**(2):241–48.
14. Hassan T, Timofeev EV, Saito T, Shimizu H, Ezura M, Matsumoto Y, Takayama K, Tominaga T, Takahashi A. A proposed parent vessel geometry-based categorization of saccular intracranial aneurysms: computational flow dynamics analysis of the risk factors for lesion rupture. *Journal of Neurosurgery* 2005; **103**(4):662–80.
15. Kim M, Taulbee DB, Tremmel M, Meng H. Comparison of two stents in modifying cerebral aneurysm haemodynamics. *Annals of Biomedical Engineering* 2008; **36**(5):726–41.
16. Satoh T, Omi M, Ohsako C, Katsumata A, Yoshimoto Y, Tsuchimoto S, Onoda K, Tokunaga K, Sugiu K, Date I. Influence of perianeurysmal environment on the deformation and bleb formation of the unruptured cerebral aneurysm: assessment with fusion imaging of 3D MR cisternography and 3D MR angiography. *American Journal of Neuroradiology* 2005; **26**:20102018.
17. Gambaruto A, Janela J, Moura A, Sequeira A. Sensitivity of haemodynamics in patient specific cerebral aneurysms to vascular geometry and blood rheology. *Mathematical Biosciences and Engineering* 2011; **8**(2):409–423.
18. Gambaruto AM, Moura A, Sequeira A. Topological flow structures and stir mixing for steady flow in a peripheral bypass graft with uncertainty. *International Journal for Numerical Methods in Biomedical Engineering* 2010; **26**(7):926–953.
19. Lee SW, Steinman DA. On the relative importance of rheology for image-based CFD models of the carotid bifurcation. *Journal of Biomedical Engineering* 2007; **129**:27378.
20. Venugopal P, Valentino D, Schmitt H, Villablanca JP, Viñuela F, Duckwiler G. Sensitivity of patient-specific numerical simulation of cerebal aneurysm haemodynamics to inflow boundary conditions. *Journal of Neurosurgery* 2007; **106**(6):1051–60.
21. Rayz VL, Boussel L, Lawton MT, Acevedo-Bolton G, Ge L, Young WL, Higashida RT, Saloner D. Numerical modeling of the flow in intracranial aneurysms: prediction of regions prone to thrombus formation. *Annals of Biomedical Engineering* 2008; **36**:1793–1804.
22. Shojima M, Oshima M, Takagi K, et al. Role of the bloodstream impacting force and the local pressure elevation in the rupture of cerebral aneurysms. *Stroke* 2005; **36**:193338.
23. Cebral JR, Castro MA, Putman CM, Alperin N. Flow-area relationship in internal carotid and vertebral arteries. *Physiological Measurement* 2008; **29**(5):585–94.
24. Janela J, Moura A, Sequeira A. Absorbing boundary conditions for a 3D non-Newtonian fluid-structure interaction model for blood flow in arteries. *International Journal of Engineering Science* 2010; **48**:1332–49.
25. Blanco PJ, Pivello MR, Urquiza SA. Feijó RA, On the potentialities of 3D–1D coupled models in haemodynamics simulations. *Journal of Biomechanics* 2009; **42**(7):919–30.
26. Peiró J, Veneziani A. Reduced models of the cardiovascular system. In *Cardiovascular Mathematics*, Formaggia L, Quarteroni A, Veneziani A (eds). Springer-Verlag: Italia, Milano, 2009.
27. Sequeira A, Moura A, Janela J. *Towards a Geometrical Multiscale Approach to Non-Newtonian Blood Flow Simulations*. Springer-Verlag: Berlin, Heidelberg, 2010. Advances in Mathematical Fluid Mechanics - dedicated to G.P. Galdi on his 60th birthday, 295–309.
28. Balossino R, Pennati G, Migliavacca F, Formaggia L, Veneziani A, Tuveri M, Dubini G. Influence of boundary conditions on fluid dynamics in models of the cardiovascular system: a multiscale approach applied to the carotid bifurcation. *Computer Methods in Biomechanics and Biomedical Engineering* 2009; **12**(1).

29. Gambaruto AM, Doorly DJ, Yamaguchi T. Wall shear stress and near-wall convective transport: comparisons with vascular remodelling in a peripheral graft anastomosis. *Journal of Computational Physics* 2010; **229**(14):5339–5356.
30. Antiga L, Piccinelli M, Botti L, Ene-Iordache B, Remuzzi A, Steinman DA. An image-based modeling framework for patient-specific computational haemodynamics. *Medical and Biological Engineering and Computing* 2008; **46**:1097–1112.
31. Gambaruto AM, Peiró J, Doorly DJ, Radaelli AG. Reconstruction of shape and its effect on flow in arterial conduits. *International Journal for Numerical Methods in Fluids* 2008; **57**:495–517.
32. Matthys KS, Alastruey J, Peiró J, Khir AW, Segers P, Verdonck PR, Parker KH, Sherwin SJ. Pulse wave propagation in a model human arterial network: assessment of 1-D numerical simulations against in vitro measurements. *Journal of Biomechanics* 2007; **40**(15):3476–3486.
33. Formaggia L, Moura A, Nobile F. On the stability of the coupling of 3D and 1D fluid-structure interaction models for blood flow simulations. *Mathematical Modelling and Numerical Analysis* 2007; **41**(4):743–769.
34. van de Vosse FN, Stergiopulos N. Pulse wave propagation in the arterial tree. *Annual Review of Fluid Mechanics* 2011; **43**(1):467–499.
35. Alastruey J, Parker KH, Peiró J, Sherwin SJ. Lumped parameter outflow models for 1-D blood flow simulations: effect on pulse waves and parameter estimation. *Communications in Computational Physics* 2008; **4**:317–336.
36. Burman E, Fernández M, Hansbo P. Continuous interior penalty finite element method for the Oseen's equations. *SIAM Journal of Numerical Analysis* 2006; **44**(3):1248–1274.
37. Hansbo P, Szepessy A. A velocity-*pressure streamline diffusion finite element method for the incompressible Navier–Stokes equations. *Computer Methods in Applied Mechanics and Engineering* 1990; **84**(2):175–192.
38. Bowker TJ, Watton PN, Summers PE, Byrne JV, Ventikos Y. Rest versus exercise hemodynamics for middle cerebral artery aneurysms: a computational study. *American Journal of Neuroradiology* 2010; **31**(2):317323.

DOI: 10.1002/cnm